Journal of Materials Chemistry A

PAPER

Cite this: J. Mater. Chem. A, 2018, 6, 932

MOF-based ternary nanocomposites for better CO_2 photoreduction: roles of heterojunctions and coordinatively unsaturated metal sites†

Xiang He and Wei-Ning Wang *

Received 18th October 2017
Accepted 4th December 2017

DOI: 10.1039/c7ta09192c

rsc.li/materials-a

Semiconductors are the most widely used catalysts for CO_2 photoreduction. However, their efficiencies are limited by low charge carrier density and poor CO_2 activation. Towards solving these issues, a metal–organic framework (MOF)-based ternary nanocomposite was synthesized through self-assembly of TiO_2/Cu_2O heterojunctions *via* a microdroplet-based approach followed by *in situ* growth of $Cu_3(BTC)_2$ (BTC = 1,3,5-benzenetricarboxylate). With increased charge carrier density and efficient CO_2 activation, the hybrid ternary nanocomposite exhibits a high CO_2 conversion efficiency and preferential formation of CH_4. Systematic measurements by using gas chromatography, photoluminescence spectroscopy, X-ray photoelectron spectroscopy, and time-resolved *in situ* diffuse reflectance infrared Fourier transform spectroscopy reveal that the semiconductor heterojunction and the coordinatively unsaturated copper sites within the hybrid nanostructure are attributable to the performance enhancements.

Introduction

Carbon dioxide (CO_2) photoreduction is a promising engineering approach to reduce atmospheric CO_2 levels and simultaneously convert CO_2 into hydrocarbon fuels.[1–9] Among the numerous catalysts for CO_2 photoreduction, semiconductors have been studied intensively because of their low cost, easy availability, nontoxicity, and exceptional chemical stability.[2,10] However, the semiconductor-based CO_2 photoreduction still suffers from low efficiency and poor selectivity, mainly due to low charge carrier density and weak ability to activate the adsorbed CO_2 molecules.

The low charge carrier density is mainly caused by inherent fast electron–hole recombination. This issue may be remediated by surface metalation,[11] where the metals serve as electron sinks to separate electron–hole pairs. Creating heterojunctions of semiconductors with proper band alignments,[12] such as TiO_2/Cu_2O,[10] Fe_2O_3/Cu_2O,[13] C_3N_4/Bi_2WO_6 [14] and ZnO/CuO,[15] is another effective approach to boost the transfer of photoexcited charge carriers between the metal oxides at the heterojunctions.[10,12] An added benefit of this type of heterojunctions is that enhanced solar energy utilization can be achieved due to the coupled narrow bandgap semiconductors, such as Cu_2O.[16]

Extensive efforts have been directed to creating semiconductor heterojunctions, many of which, however, require complicated processes.[10,17] In addition, many heterojunctions are fabricated in the form of a "core–shell" structure, that is, one semiconductor layer is uniformly coated on the other.[10] This significantly limits the use of heterojunctions, since in many cases, the surfaces of both semiconductors are required to participate in the redox reactions.[12] Moreover, despite the promise of enhanced charge transfer, the semiconductor heterojunctions still suffer from poor CO_2 adsorption and activation due to the low affinity of CO_2 molecules to the semiconductor surface.[18] Rational design of photocatalysts for efficient CO_2 photoreduction is thus highly desirable.

On the other hand, metal–organic frameworks (MOFs), as an emerging class of highly porous materials, have received increasing attention in CO_2 photoreduction,[19–23] mainly due to their high surface area, tunable pore size, and rich surface functionality. Given the exceptional gas adsorption ability of MOFs, many current studies are focusing on designing MOFs/semiconductor hybrids to enhance the gas uptake during CO_2 photoreduction.[20,24] For example, hybrid nanorods of the Zn_2GeO_4/zeolitic imidazolate framework (ZIF)-8 exhibited 1.62 times higher CO_2 photoreduction efficiency than that of bare Zn_2GeO_4,[25] attributed to the enhancement in the CO_2 adsorption capacity after the incorporation of ZIF-8. Similarly, C_3N_4/ZIF-8 composite nanotubes were reported to have a better CO_2 photoreduction performance than pristine C_3N_4, where the enhanced CO_2 adsorption capacity due to ZIF-8 was the main

Department of Mechanical and Nuclear Engineering, Virginia Commonwealth University, Richmond, Virginia 23219, USA. E-mail: wnwang@vcu.edu

† Electronic supplementary information (ESI) available: Characterization of TiO_2 and Cu_2O, additional SEM images, determination of component ratio, CO_2 uptake analysis, CO_2 photoreduction analysis, analysis of Cu valence states after photocatalysis, photoluminescence spectra of photo-generated 7-hydroxycoumarin, calibration curve of photoluminescence intensity *versus* $^{\cdot}OH$ concentration and water adsorption analysis. See DOI: 10.1039/c7ta09192c

reason.[24] Besides ZIF-8, other MOFs were also used to increase the CO_2 adsorption ability of the catalysts.[26]

It should be noted that, adsorption is the first step in CO_2 photoreduction. Whether and how the adsorbed CO_2 molecules are activated and then reduced within the MOF structure are also of great importance to study. In particular, some MOFs (*e.g.*, $Cu_3(BTC)_2$, BTC = 1,3,5-benzenetricarboxylate) have coordinatively unsaturated metal sites, which could act as electron donors to activate the adsorbed gas molecules.[27] However, little attention has been paid to this area.

Towards addressing the aforementioned long-standing issues in CO_2 photoreduction (*i.e.*, low charge carrier density and inefficient CO_2 activation), we herein report a rational development of MOF-based ternary nanocomposites composed of TiO_2/Cu_2O heterojunctions and $Cu_3(BTC)_2$, where the roles of the heterojunctions and MOF in charge transfer and CO_2 activation are systematically explored. Specifically, the nanocomposites were synthesized *via* rapid self-assembly of TiO_2/Cu_2O nanoparticles within microdroplets,[28,29] followed by *in situ* growth of $Cu_3(BTC)_2$ on the TiO_2/Cu_2O surface, where part of Cu_2O serves as the sacrificial copper source. The overall synthetic procedure of the $TiO_2/Cu_2O/Cu_3(BTC)_2$ ternary nanocomposites is illustrated in Scheme 1 and detailed in the Experimental section. The unique ternary $TiO_2/Cu_2O/Cu_3(BTC)_2$ composite possesses heterojunctions and abundant coordinatively unsaturated copper sites, which results in not only increased charge carrier density but also efficient activation of CO_2 molecules, therefore leading to high CO_2 conversion efficiency and preferential formation of CH_4. With systematic measurements and analyses, a plausible pathway of CO_2 activation and subsequent reduction in this ternary system was proposed. The outcome of this work provides new insights into rational design of MOF-based hybrid nanomaterials for efficient CO_2 photoreduction.

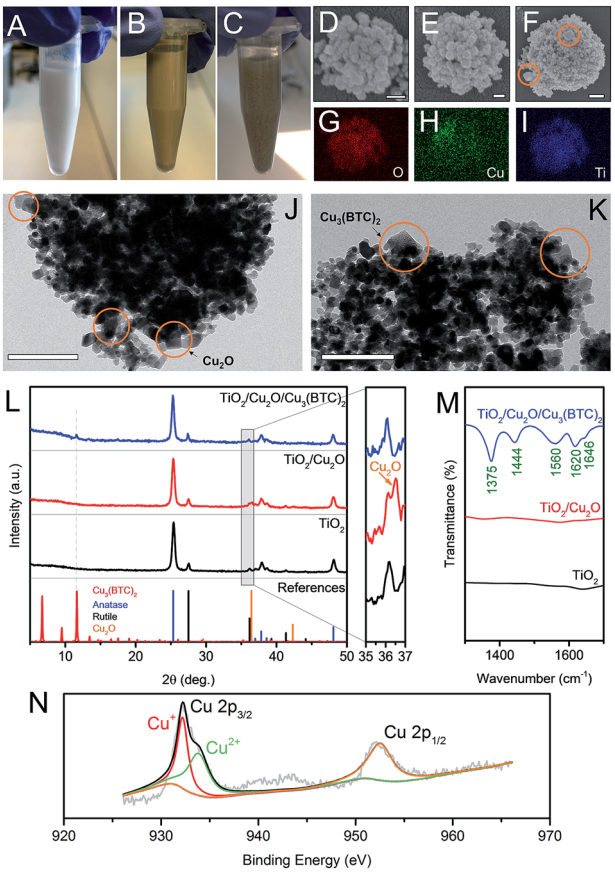

Fig. 1 Digital images of aqueous suspensions containing (A) as-sprayed TiO_2, (B) TiO_2/Cu_2O, and (C) $TiO_2/Cu_2O/Cu_3(BTC)_2$; SEM images of (D) as-sprayed TiO_2, (E) TiO_2/Cu_2O and (F) $TiO_2/Cu_2O/Cu_3(BTC)_2$ samples; (G)–(I) EDX mapping images of TiO_2/Cu_2O particles; TEM images of (J) TiO_2/Cu_2O and (K) $TiO_2/Cu_2O/Cu_3(BTC)_2$; XRD patterns (L) and FT-IR spectra (M); (N) Cu2p XPS spectra of the as-prepared $TiO_2/Cu_2O/Cu_3(BTC)_2$ composite (scale bars: (D and E) 100 nm; (F) 300 nm; (J and K) 200 nm).

Results and discussion

Materials characterization

The representative samples, *i.e.*, the as-sprayed TiO_2, TiO_2/Cu_2O, and $TiO_2/Cu_2O/Cu_3(BTC)_2$, were first subjected to detailed characterization. As shown in the digital images (Fig. 1A–C), the color change of the samples is apparent. The white color of TiO_2 (Fig. 1A) turned yellow with the incorporation of Cu_2O (Fig. 1B) due to its broad light absorption between 350 nm and 500 nm (Fig. S1E†). After partial conversion of Cu_2O to $Cu_3(BTC)_2$, the color of the nanocomposite changed to gray (Fig. 1C). The low-magnification scanning electron microscopy (SEM) images (Fig. S2†) show that all three samples are relatively homogeneous. The high-magnification SEM analysis reveals that the as-sprayed TiO_2 and TiO_2/Cu_2O particles have a spherical shape (Fig. 1D and E), resulting from the one droplet to one particle conversion principle.[28] The existence of Cu elements in the TiO_2/Cu_2O composite was confirmed by energy dispersive X-ray (EDX) analysis (Fig. 1G–I). Cu_2O nanocubes are also found in Fig. 1J, where free surfaces are available for the subsequent growth of $Cu_3(BTC)_2$. After the growth of $Cu_3(BTC)_2$, the spherical shape was largely maintained (Fig. 1F). The octahedral $Cu_3(BTC)_2$ crystals are clearly observed from both the SEM (Fig. 1F) and transmission electron microscopy (TEM) images (Fig. 1K). The existence of Cu_2O and $Cu_3(BTC)_2$ in the composite was further identified by X-ray diffraction (XRD) analysis (Fig. 1L). For example, Cu_2O in the TiO_2/Cu_2O composite was confirmed by the peak of the (111) plane at 36.5° (see also Fig. S1D†), the intensity of which decreased after the growth of $Cu_3(BTC)_2$. The presence of $Cu_3(BTC)_2$ in the ternary

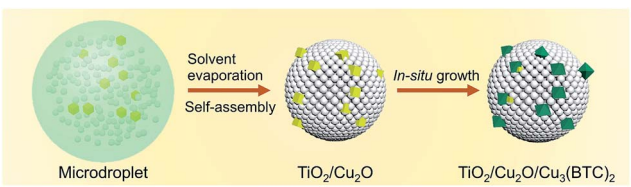

Scheme 1 Schematic illustration of the experimental procedure to synthesize $TiO_2/Cu_2O/Cu_3(BTC)_2$ ternary nanocomposites (white spheres: TiO_2; yellow cubes: Cu_2O; green octahedra: $Cu_3(BTC)_2$).

composite is evidenced by its main XRD peak at $2\theta = \sim 11.6^\circ$, corresponding to its (222) plane.[21,30] Besides, the Fourier transform infrared (FT-IR) spectra also confirm the successful growth of $Cu_3(BTC)_2$, where the intense peaks were observed at 1375, 1444, 1560, 1620 and 1646 cm^{-1}, assigned to carboxylate groups of $Cu_3(BTC)_2$.[31,32] It should be noted that both XRD peaks of Cu_2O and $Cu_3(BTC)_2$ are relatively weak due to their low molar ratios. These were intentionally set to minimize the influence of adsorption variation (see Fig. S3†), in order to better understand the roles of TiO_2/Cu_2O heterojunctions and $Cu_3(BTC)_2$ in the enhancements of charge carrier density and CO_2 molecule activation during CO_2 photoreduction. In addition, the valence states of Cu in the ternary composite analyzed by X-ray photoelectron spectroscopy (XPS) further confirm the coexistence of Cu_2O and $Cu_3(BTC)_2$ in the ternary system. As shown in Fig. 1N, two major peaks were observed at 932.3 eV and 952.5 eV, corresponding to Cu $2p_{3/2}$ and Cu $2p_{1/2}$, respectively. The Cu $2p_{3/2}$ was further deconvoluted into two peaks centered at 932.2 eV and 933.8 eV, originating from Cu^+ in Cu_2O and Cu^{2+} in $Cu_3(BTC)_2$, respectively.[33,34] Furthermore, based on the precursor components and the XPS data, the molar ratio of TiO_2, Cu_2O and $Cu_3(BTC)_2$ in the ternary composite was determined to be 20 : 0.55 : 0.45 (ESI, S4†).

CO_2 photoreduction analysis

The CO_2 photoreduction was carried out in a continuous-flow mode. The analysis procedures were detailed in our previous studies[21,35] and are described briefly in the Experimental section. Prior to CO_2 photoreduction analysis, all samples were subjected to control measurements under a helium/water atmosphere to rule out the possibilities of carbon contamination (Fig. S4A–E†). The CO_2 photoreduction analysis results indicate that pure $Cu_3(BTC)_2$ doesn't serve as the photocatalyst for CO_2 reduction (Fig. S5†) due to the unfavorable charge separation,[19,21] while TiO_2 and the composite reduce CO_2 to carbon monoxide (CO) and methane (CH_4) (Fig. S4F–H†). Specifically, the CO and CH_4 yields of the sprayed TiO_2 were 72 and 33 μmol h^{-1} g^{-1}, respectively (Fig. 2). With the incorporation of Cu_2O, the yields were increased to 155 and 85 μmol h^{-1} g^{-1}, respectively. In the case of the ternary composite, the CO yield was increased more than 2-fold, while the CH_4 yield was almost 4 times higher than that of TiO_2. It's worth noting that, besides the overall production yields, the preferential formation of CH_4 was also enhanced along with the sample development. For example, the CH_4/CO ratio in the case of TiO_2 was only 0.46. With the incorporation of Cu_2O and $Cu_3(BTC)_2$, the CH_4/CO ratio was improved to 0.55 and 0.77, respectively (Fig. 2). Moreover, the Cu valence states are relatively stable during the CO_2 photoreduction process, as evidenced by similar Cu 2p spectra of the ternary composite before and after 7-hour photocatalysis (Fig. 1N and S6†).

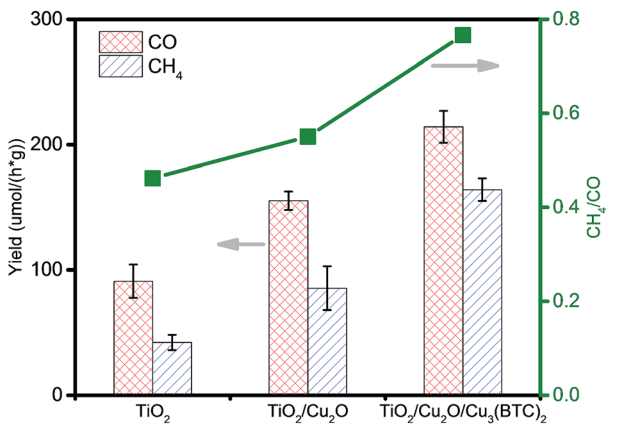

Fig. 2 Analysis of CO_2 photoreduction product yields.

There are several possible reasons for the enhanced CO_2 photoreduction with the incorporation of Cu_2O and $Cu_3(BTC)_2$, including higher CO_2 uptake, enhanced charge carrier density, and improved CO_2 activation. In this study, the interference from the changes in the CO_2 uptake capacity may be negligible since the amounts of Cu_2O and $Cu_3(BTC)_2$ in the nanocomposites were controlled at very low percentages, which ensures minimal improvement in CO_2 uptake (Fig. S3†). While, the contributions from the increased charge carrier density and facile activation of the adsorbed CO_2 molecules are discussed in detail as follows.

Analysis of charge carrier density

To understand the roles of the Cu_2O and $Cu_3(BTC)_2$ in the increment of charge carrier density, quantitative measurements of charge carrier generation were carried out. In this study, a convenient and reliable photoluminescence (PL) technique using coumarin as a probe molecule to detect and quantify photoinduced holes was used.[36–38] In this method, coumarin reacts with hydroxyl radicals (•OH), produced from the reaction of photoinduced holes with water molecules adsorbed on the photocatalyst surface, to form highly fluorescent 7-hydroxycoumarin (7HC), which has a characteristic PL emission peak at around 455 nm when excited at 350 nm (Fig. S7 and S8†). In the current study, all three samples have similar water adsorption capacities (Fig. S10†), thus the amount of hydroxyl radicals can be used to indicate the density of the holes.

As shown in Fig. 3A and S9,† the as-sprayed TiO_2 demonstrates a low charge carrier density as no apparent peak at 455 nm was observed. With the incorporation of Cu_2O, the 7HC peak is prominent (Fig. 3B). The strongest 7HC peak intensity is found in Fig. 3C, where the ternary nanocomposite was used. Based on the calibration results (Fig. S8†), the OH generated by TiO_2, TiO_2/Cu_2O and $TiO_2/Cu_2O/Cu_3(BTC)_2$ was quantified to be 0.032, 0.067 and 0.105 μmol g^{-1} h^{-1}, respectively, which implies that the photo-induced holes in TiO_2/Cu_2O and $TiO_2/Cu_2O/Cu_3(BTC)_2$ were 2.09 and 3.28 times higher than those in TiO_2.

The above results indicate that the decoration of TiO_2 with Cu_2O and $Cu_3(BTC)_2$ significantly increased the charge carrier density of the catalyst, which might be attributed to several reasons, including the enhanced light absorption and promoted electron/hole separation. The light absorption properties of the three samples were assessed by using the UV-Vis absorption spectra as shown in Fig. 4. Specifically, TiO_2 only

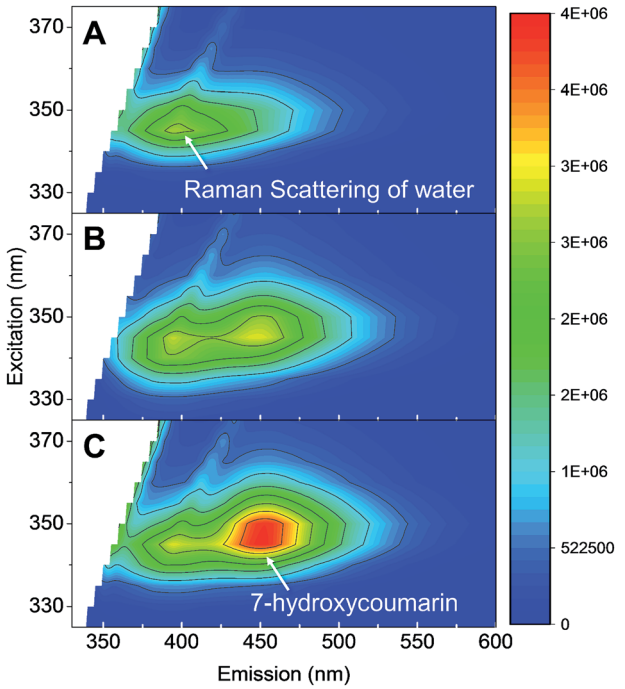

Fig. 3 Excitation–emission matrices of 7-hydroxycoumarin washed off from catalysts after CO_2 photoreduction in the presence of coumarin: (A) as-sprayed TiO_2, (B) TiO_2/Cu_2O and (C) $TiO_2/Cu_2O/Cu_3(BTC)_2$.

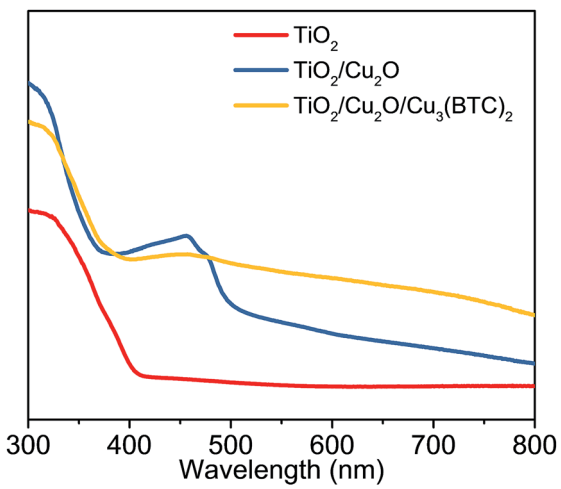

Fig. 4 UV-Vis spectra of the samples.

exhibits light absorption in the UV region (<400 nm). With the incorporation of Cu_2O, a new absorption peak was observed from 350 to 500 nm, consistent with the yellow color of the TiO_2/Cu_2O composite. After the partial conversion of Cu_2O to $Cu_3(BTC)_2$, the ternary composite shows a broad absorption peak from 400 nm to 800 nm, suggesting the utilization of visible light for the enhanced charge carrier density.

In addition to the light absorption, the band alignment between TiO_2 and Cu_2O is also critical for the charge carrier density. Herein, the method proposed by Kraut *et al.*[39] was applied to figure out the precise band alignment between TiO_2 and Cu_2O. Specifically, XPS measurements were conducted to acquire the core-level energy and upper edge of the valence band (VB) (Fig. 5A–C), meanwhile, the information from the UV-Vis analysis (Fig. 4 and S1E†) was used to derive the band gaps (BGs) (Fig. 5D). The valence band offset, VBO, could be determined from the following equation,

$$\mathrm{VBO} = (E^{\mathrm{bulk}}_{\mathrm{Cu\text{-}core}} - E^{\mathrm{bulk}}_{\mathrm{Cu\text{-}valence}}) - (E^{\mathrm{bulk}}_{\mathrm{Ti\text{-}core}} - E^{\mathrm{bulk}}_{\mathrm{Ti\text{-}valence}}) - (E^{\mathrm{composite}}_{\mathrm{Cu\text{-}core}} - E^{\mathrm{composite}}_{\mathrm{Ti\text{-}core}}) \quad (1)$$

while, the conduction band offset, CBO, could be calculated using the equation below based on the result from eqn (1).

$$\mathrm{CBO} = \mathrm{BG}_{\mathrm{Cu_2O}} + \mathrm{VBO} - \mathrm{BG}_{\mathrm{TiO_2}} \quad (2)$$

where $E^{\mathrm{bulk}}_{\mathrm{Cu\text{-}core}}$ and $E^{\mathrm{bulk}}_{\mathrm{Ti\text{-}core}}$ are the core-level energies of pure bulk Cu_2O and TiO_2, respectively; $E^{\mathrm{bulk}}_{\mathrm{Cu\text{-}valence}}$ and $E^{\mathrm{bulk}}_{\mathrm{Ti\text{-}valence}}$ indicate the upper edges of VBs of Cu_2O and TiO_2, respectively; $E^{\mathrm{composite}}_{\mathrm{Cu\text{-}core}} - E^{\mathrm{composite}}_{\mathrm{Ti\text{-}core}}$ indicates the core-level energy differences in the TiO_2/Cu_2O composite.

With aforementioned information, the precise band alignment in the TiO_2/Cu_2O heterojunction was obtained and is schematically shown in Fig. 5E. With a more negative conduction band of Cu_2O, the photogenerated electrons on Cu_2O can migrate to TiO_2 for CO_2 reduction. On the other hand, the accumulated holes flow in the opposite direction for water oxidation to release H^+ and O_2.[40] The efficient transfer of charge carriers between TiO_2 and Cu_2O highly remediates the electron–hole recombination and contributes to the higher charge carrier density.

When Cu_2O was partially converted to $Cu_3(BTC)_2$, the electron–hole separation was further enhanced. In particular, $Cu_3(BTC)_2$ itself is unfavorable for charge separation as demonstrated by the ultrafast transient absorption spectroscopy analysis.[19] However, the photoinduced electrons can effectively transfer from semiconductors to the coordinatively unsaturated copper sites in $Cu_3(BTC)_2$, suppressing the electron–hole recombination,[19] which is in agreement with the experimental results of $^{\bullet}OH$ formation. The mechanism of the charge transfer between semiconductor composites and $Cu_3(BTC)_2$ is schematically shown in Fig. 5E.

CO_2 molecule activation analysis

In addition to the enhanced charge carrier density, the CO_2 molecule activation also plays an important role in the promotion of CO_2 photoreduction efficiency of the ternary nanocomposites. In the present work, CO_2 activation is evidenced by various intermediates formed during the CO_2 adsorption process (Fig. 6), which was analyzed by time-resolved *in situ* diffuse reflectance infrared Fourier transform spectroscopy (DRIFTS). As shown in Fig. 6A, the adsorbed water molecules are dominant on the pristine TiO_2 surface (1640 cm^{-1}),[41] along with a small amount of bidentate carbonate (b-CO_3^{2-}, 1325 and 1585 cm^{-1})[42,43] and monodentate bicarbonate (m-HCO_3^-, 1405 cm^{-1})[44] (Fig. 6B). With the incorporation of Cu_2O, the intermediates were dominated by b-

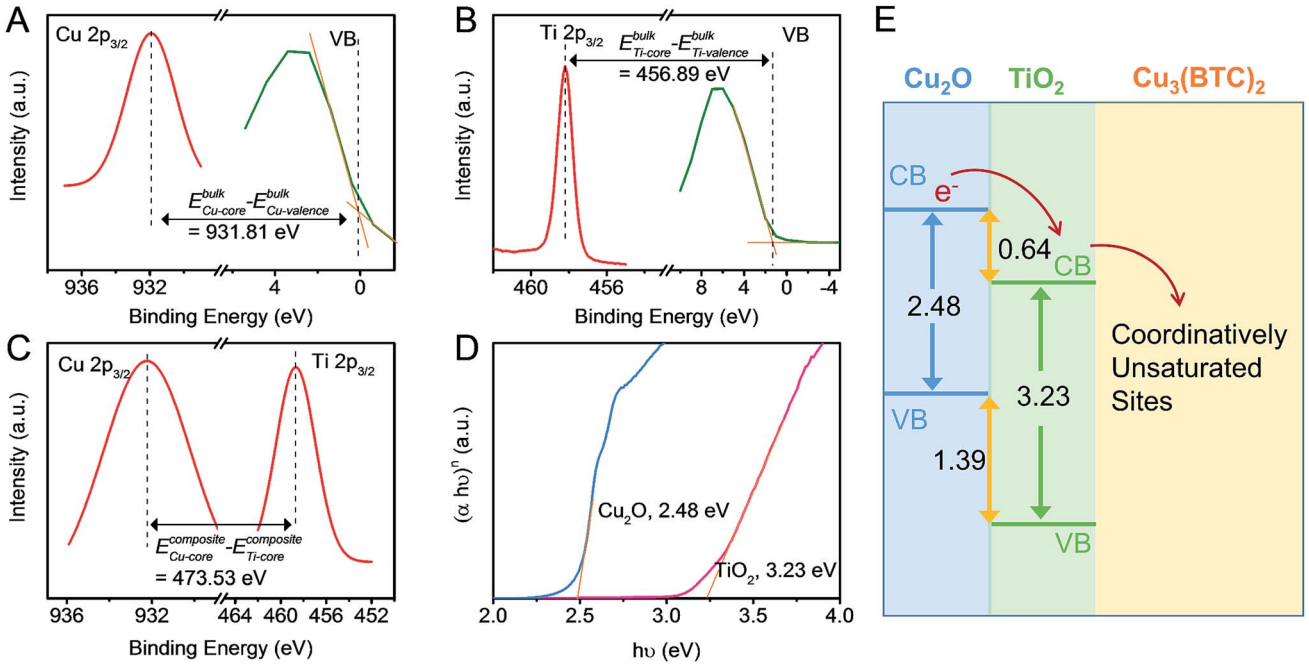

Fig. 5 XPS valence band and core-level spectra of (A) pure bulk Cu_2O, (B) pure bulk TiO_2 and (C) TiO_2/Cu_2O composite; (D) Tauc plots of pure bulk Cu_2O and TiO_2; (E) schematic illustration of charge transfer in $TiO_2/Cu_2O/Cu_3(BTC)_2$ (unit: eV).

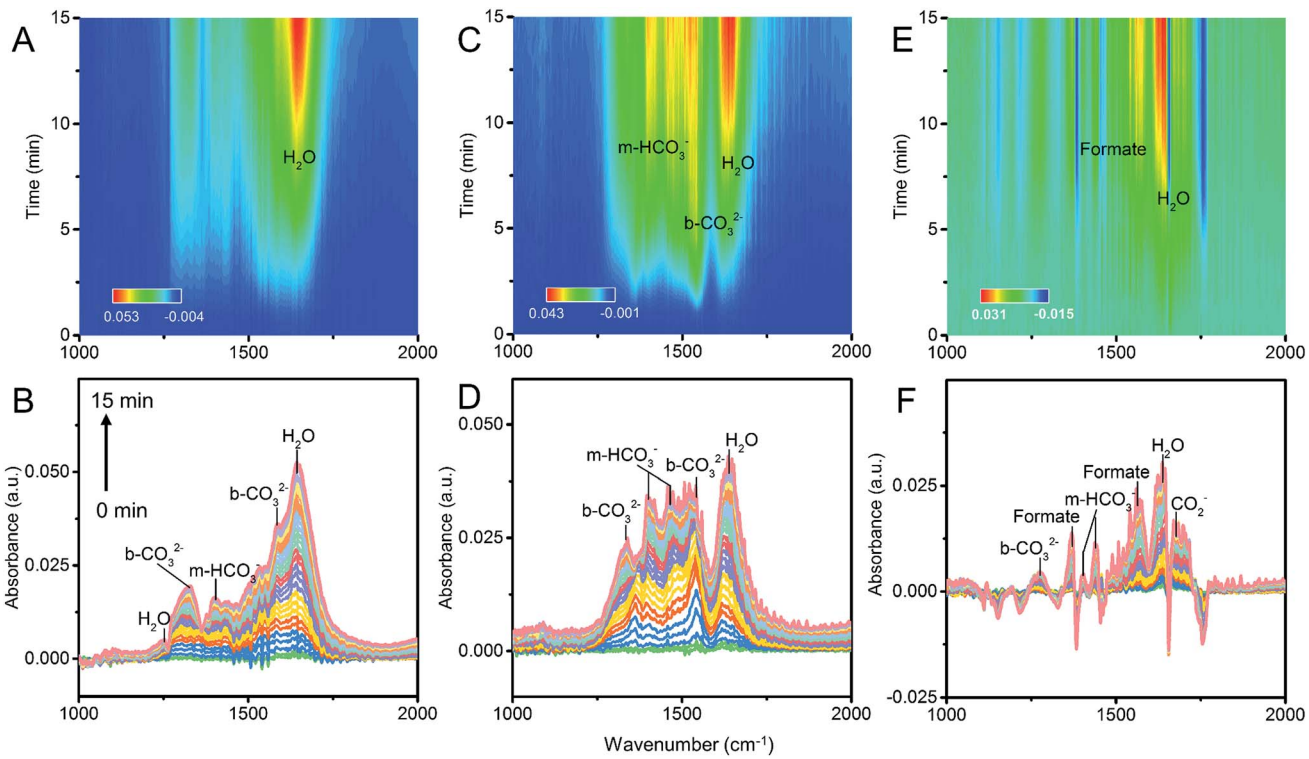

Fig. 6 DRIFTS spectra recorded during the adsorption of the CO_2/water mixture on sprayed TiO_2 (A and B), TiO_2/Cu_2O (C and D) and $TiO_2/Cu_2O/Cu_3(BTC)_2$ (E and F). Top panel: 2D view and bottom panel: the corresponding spectra.

CO_3^{2-} (1334 and 1543 cm^{-1})[43,45] and monodentate HCO_3^- (1405 cm^{-1} and 1464 cm^{-1})[44,46] (Fig. 6C and D). Compared with b-CO_3^{2-}, m-HCO_3^- is more active and can easily be converted to hydrocarbons.[47] It's worth noting that the percentage of m-HCO_3^- on TiO_2/Cu_2O is larger than that on TiO_2, indicating the enhanced activation ability of the catalyst with the

incorporation of Cu_2O, which contributed to the increased CO_2 photoreduction efficiency. Furthermore, after the partial conversion of Cu_2O to $Cu_3(BTC)_2$, the intermediates were dominated by CO_2^- (1677 cm^{-1})[42] and bridging bidentate formate (1563 and 1370 cm^{-1})[48] (Fig. 6E and F). Notably, CO_2^- and formate are even more active than m-HCO_3^-, which can easily be transformed into the products upon photo-irradiation.[49] The relative activities of the formed intermediates agree well with the corresponding CO_2 photoreduction performance (Fig. 2), which confirms the importance of CO_2 molecule activation in the CO_2 photoreduction process in this work.

The formation of various intermediate species is related to the abundance of the coordinatively unsaturated (or open) metal sites in the catalysts. These open metal sites could induce multipole moments in CO_2 molecules and enhance the electrostatic interactions between them, resulting in the activation of CO_2 molecules.[50] As evidenced by the XRD measurements (Fig. S1D†), the Cu_2O nanoparticles are dominated by (111) facets, where twenty-five percent of the copper ions are coordinatively unsaturated.[51] Compared with Cu_2O, $Cu_3(BTC)_2$ has more coordinatively unsaturated copper sites, arising from the unique structure of the framework.[52] Therefore, the incorporation of these two components brings extra open metal sites to the system, which significantly changes intermediate species during the CO_2 adsorption process. The formation mechanisms of two typical intermediates (*i.e.*, m-HCO_3^- and formate) are proposed as follows and schematically shown in Fig. 7.

In general, during the co-adsorption of CO_2 and H_2O on the semiconductors, CO_2 interacts with the coordinatively unsaturated metal sites in a tilted linear configuration, while H_2O dissociates into hydroxyls (see Fig. S10† for more information). The linear CO_2 then reacts with hydroxyls to form m-HCO_3^- (Fig. 7A). The incorporation of Cu_2O led to slightly increased coordinatively unsaturated metal sites, and subsequently enhanced the interaction of CO_2 with the metal sites, thus promoting the formation of m-HCO_3^- (Fig. 6C and D). After partial conversion of Cu_2O to $Cu_3(BTC)_2$, the amount of coordinatively unsaturated copper sites increased significantly, leading to a bent CO_2 configuration.[50] The bent configuration makes CO_2 act as an anionic molecule, resulting in the localization of negative charge in the carbon atom of the CO_2 molecule. The terminal oxygen then gains negative charge with the electron transferred from the coordinatively unsaturated copper sites due to the charge polarization.[27] With the electrons transferred to the lowest unoccupied molecular orbital (LUMO), the adsorbed CO_2 can then be activated to CO_2^-.[53] In the presence of protons derived from the dissociative water adsorption (see Fig. S10C† for more information), the adsorbed CO_2 would be activated to formate (Fig. 7B). In the meantime, the co-adsorption of water can also help to stabilize the active intermediates through hydrogen bonding.[27]

The preferential adsorption sites for CO_2 can be indirectly assessed by observing the CO_2 adsorption modes with the aid of the DRIFTS analysis (Fig. 8). As shown in Fig. 8A, the adsorbed CO_2 molecules have two major characteristic peaks. The peak centered at 2360 cm^{-1} is attributed to the functional group ···O═C═O adducts formed by the interaction of CO_2 with the functional groups.[54] While, the peak centered at 2340 cm^{-1} with a frequency shoulder at 2330 cm^{-1} originates from the ν_3 mode of CO_2 interacting with the coordinatively unsaturated metal sites.[55,56] In addition, the peak area is associated with the amount of adsorbed CO_2. Thus, it is rational to estimate the preferential adsorption sites for the CO_2 molecules by using the area ratios of the peaks centered at 2340 cm^{-1} to those at 2360 cm^{-1}. As shown in Fig. 8B, the highest peak ratios were found for the $TiO_2/Cu_2O/Cu_3(BTC)_2$ ternary nanocomposites, indicating the existence of ample coordinatively unsaturated copper sites in the structure, which contribute to the subsequent charge separation and CO_2 activation, and hence the improvement of overall CO_2 photoreduction performance.

Taken together, a CO_2 photoreduction mechanism of using the MOF-based ternary nanocomposites is proposed in Scheme 2 and descried as follows. Initially, CO_2 molecules interact with various adsorption sites, including Ti, Cu and surface functional groups. The presence of Cu_2O and $Cu_3(BTC)_2$ in the ternary system introduces abundant coordinatively unsaturated copper sites, which can activate the adsorbed CO_2 molecules to form active intermediates, including formate species and CO_2^-. Upon light irradiation, these active intermediates are converted to products with sufficient supply of electrons resulting from the enhanced light absorption and the efficient charge separation. In particular, the preferential formation of CH_4 originates from the existence of formate species, which are sequentially

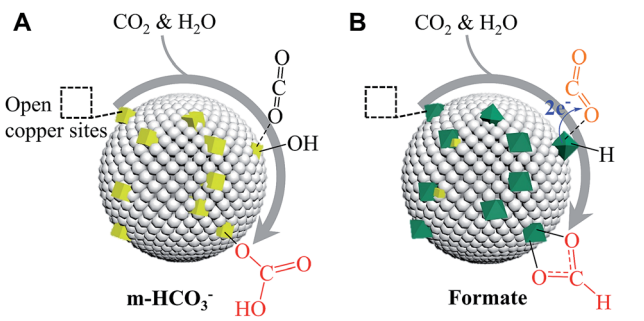

Fig. 7 Proposed mechanisms for the formation of (A) m-HCO_3^- and (B) formate (white spheres: TiO_2; yellow cubes: Cu_2O; green octahedra: $Cu_3(BTC)_2$).

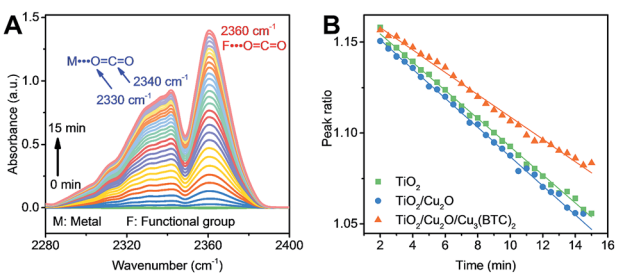

Fig. 8 (A) DRIFTS spectra in the range of 2280 to 2400 cm^{-1} obtained during the adsorption of the CO_2/H_2O mixture on the $TiO_2/Cu_2O/Cu_3(BTC)_2$ surface; (B) peak area ratios ($peak_{2340}/peak_{2360}$) of the three representative samples.

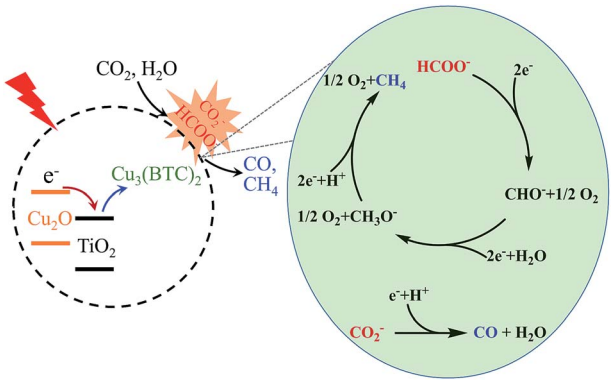

Scheme 2 The proposed reaction pathways in the MOF-based ternary photocatalyst system.

reduced to CHO^-, CH_3O^-, and CH_4 upon light irradiation (Scheme 2), where each step involves the transfer of two electrons.[57,58] The proposed pathway requires only six electrons, which is energetically favorable as compared to the conventional eight-electron process of direct reduction of CO_2 to CH_4.[3,7] On the other hand, CO is generated from CO_2^- (Scheme 2), which only requires one electron.[1,2] Another pathway where CH_4 is formed with CO being the intermediate, which usually occurs on the metal-coated photocatalysts,[35,59,60] is unlikely in this work, since the CO evolution in the ternary system was not suppressed along with the promotion of CH_4 formation (Fig. 2).

Conclusions

In summary, a MOF-based ternary composite photocatalyst ($TiO_2/Cu_2O/Cu_3(BTC)_2$) was designed towards enhanced CO_2 photoreduction by increasing the charge carrier density and facilitating the CO_2 molecule activation. Systematic CO_2 photoreduction analyses were carried out to unravel the mechanisms. The results show that the incorporation of Cu_2O and $Cu_3(BTC)_2$ not only significantly improved the overall CO_2 photoconversion efficiency, but also led to the preferential formation of CH_4. The enhanced performance of the catalysts stems from the increased charge carrier density and efficient CO_2 activation by coordinatively unsaturated metal sites as verified and quantified by PL, XPS, and DRIFTS measurements. This work demonstrates a novel strategy to address low charge density and inefficient CO_2 activation issues, and meanwhile provides insights into the rational design of MOF-based hybrid nanomaterials for CO_2 photoreduction and other applications.

Experimental

Synthetic procedures

All chemicals were purchased from commercial suppliers (Sigma-Aldrich, VWR, Acros Organics) and used as received without further purification.

(1) Synthesis of Cu_2O nanocubes. The Cu_2O nanocubes were synthesized as previously published:[61] 1 mL $CuSO_4$ solution (1.2 mol L^{-1}) was firstly added into 400 mL deionized (DI) water. Then, NaOH (1 mL, 4.8 mol L^{-1}) and ascorbic acid (1 mL, 1.2 mol L^{-1}) were injected into the solution after 5 min and 10 min, respectively. The solution was then aged for 30 min. All the above processes were done under vigorous stirring at room temperature. After that, the Cu_2O nanocubes were collected and washed four times with DI water *via* centrifugation and redispersion to ensure the complete removal of residues. Characterization of the as-synthesized Cu_2O is provided in the ESI, S1.†

(2) Aerosol-assisted synthesis of TiO_2/Cu_2O composites. TiO_2/Cu_2O composites were assembled *via* the aerosol process as detailed in our previous studies.[28] Briefly, aqueous solution containing TiO_2 nanoparticles (0.05 mol L^{-1}, Degussa (Evonik) P25, see S1† for characterization) and Cu_2O nanocubes (0.0025 mol L^{-1}) was used as the precursor, from which microdroplets were generated using a Collison nebulizer. The droplets were then carried through a furnace (400 °C) by air (10 L min^{-1}). During the flying process, the droplets underwent solvent evaporation and self-assembly of Cu_2O and TiO_2 nanoparticles. The TiO_2/Cu_2O composites were collected in the downstream of the furnace by using a micro-filter.

(3) *In situ* growth of MOFs. The as-prepared TiO_2/Cu_2O composite was then put into the BTC solution (0.04 mol L^{-1}, $V_{EtOH}/V_{H_2O} = 9/1$), which was then subjected to vortex mixing for 0.5 min to partially convert Cu_2O to $Cu_3(BTC)_2$ and obtain the $TiO_2/Cu_2O/Cu_3(BTC)_2$ composites. After that, the final product was immediately collected and washed with ethanol four times to remove the residuals *via* centrifugation/redispersion and then dried in a vacuum at 50 °C.

Materials characterization

The morphologies and inner structures of the samples were characterized by using a scanning electron microscope (SEM, Su-70, Hitachi) and a transmission electron microscope (TEM, JEM 1230, JEOL), respectively. A PANalytical X'Pert Pro MPD X-ray diffractometer equipped with a Cu-Kα radiation source ($\lambda = 1.5401$ Å) was used for the crystallinity determination. The surface functional groups were analyzed by using a Fourier transform infrared (FT-IR) spectrometer (Nicolet iS50, Thermo Scientific). X-ray photoelectron spectroscopy (XPS) measurements were carried out by using a Thermofisher ESCALab 250. A UV-Visible spectrophotometer (Evolution 220, ThermoFisher) was used to obtain the optical properties of the samples.

CO_2 photoreduction analysis

The CO_2 photoreduction was carried out in a continuous-flow mode and the analysis procedures were detailed in our previous studies.[21] In brief, the CO_2/H_2O mixture was generated by passing CO_2 gas (purity > 99.99%, Praxair) through a water bubbler. The gas mixture, serving as the reactants, was then introduced into a home-made photoreactor loaded with catalysts. The photoreactor consists of a cylindrical cavity made of stainless steel (60 mm in diameter and 25 mm in depth) and a quartz glass for the light to pass. The light illumination was provided by a Xe lamp (450 W, Newport). The reactor was first purged with the gas mixture with a flow rate of 50 mL min^{-1} for 30 min. The flow rate of the gas mixture was then reduced to 3

mL min^{-1} and the lamp was turned on for the photoreduction process. The effluent gases were analyzed by using a gas chromatograph (GC, Agilent 7890B) equipped with a CarboPLOT P7 column and a thermal conductivity detector (TCD). For each sample, the analysis was conducted three times to obtain the average production yield. A liquid filter (6123NS, Newport) was used to minimize the thermal effects. As reported in our previous work where the same apparatus was used,[35] the reactor temperature can be controlled within 32 °C with the aid of the filter, limiting the thermal contributions to CO_2 photoreduction. In order to rule out any possibilities of carbon contamination, control experiments were conducted with the same procedures using helium gas (purity > 99.995%, Praxair) instead of CO_2 (see Fig. S4† for details).

Hydroxyl radicals (˙OH) analysis

The detection of ˙OH was conducted using the same procedure as the CO_2 photoreduction but with the mixtures of catalysts (1 mg) and coumarin (10 mg). During the illumination process, ˙OH radicals are formed through the reaction of holes with water molecules adsorbed on the catalyst surfaces. These radicals then react with coumarin, producing 7-hydroxycoumarin, which has a characteristic fluorescence peak around 455 nm when excited at 350 nm (Fig. S7†). After the completion of the photocatalysis process, the powder mixtures were dispersed in 4 mL DI water to extract 7-hydroxycoumarin. The powders were then removed by centrifugation. And the suspension was analyzed by using a fluorescence spectrofluorometer (QuantaMaster 400, Photon Technology International).

Time-resolved *in situ* diffuse reflectance infrared Fourier transform spectroscopy (DRIFTS) analysis

The DRIFTS analysis was conducted in a reaction chamber assembled in a Praying Mantis diffuse reflection accessory of the FT-IR spectrometer (i50, Thermo Scientific). The experimental procedure involves two steps, *i.e.*, purging and CO_2 adsorption. In brief, photocatalysts were firstly loaded in the reaction chamber and then subjected to purging under helium gas flow (30 mL min^{-1}) at 150 °C for 30 min in order to further remove any residual hydrocarbons. After that, the heater was turned off and the chamber was cooled down to room temperature. Helium gas flow was stopped and CO_2 gas flow (10%, helium as the balance gas) was introduced into the reaction chamber at a flow rate of 4 mL min^{-1} after passing through the water bubbler. The IR spectra were recorded as a function of adsorption time.

Conflicts of interest

There are no conflicts to declare.

Acknowledgements

This study was supported by the Donors of the American Chemical Society (ACS) Petroleum Research Fund (57072-DNI10), the National Science Foundation (CMMI-1727553), and the Virginia Commonwealth University (VCU) Presidential Research Quest Fund. We thank Dr Dawei Wang for TEM measurements, which were carried out at the VCU Department of Anatomy and Neurobiology Microscopy Facility, with funding from the NIH-NINDS Centre core grant (5P30NS047643).

Notes and references

1 P. Usubharatana, D. McMartin, A. Veawab and P. Tontiwachwuthikul, *Ind. Eng. Chem. Res.*, 2006, **45**, 2558–2568.
2 V. P. Indrakanti, J. D. Kubicki and H. H. Schobert, *Energy Environ. Sci.*, 2009, **2**, 745–758.
3 S. C. Roy, O. K. Varghese, M. Paulose and C. A. Grimes, *ACS Nano*, 2010, **4**, 1259–1278.
4 A. Dhakshinamoorthy, S. Navalon, A. Corma and H. Garcia, *Energy Environ. Sci.*, 2012, **5**, 9217–9233.
5 E. V. Kondratenko, G. Mul, J. Baltrusaitis, G. O. Larrazabal and J. Perez-Ramirez, *Energy Environ. Sci.*, 2013, **6**, 3112–3135.
6 S. N. Habisreutinger, L. Schmidt-Mende and J. K. Stolarczyk, *Angew. Chem., Int. Ed.*, 2013, **52**, 7372–7408.
7 J. L. White, M. F. Baruch, J. E. Pander, Y. Hu, I. C. Fortmeyer, J. E. Park, T. Zhang, K. Liao, J. Gu, Y. Yan, T. W. Shaw, E. Abelev and A. B. Bocarsly, *Chem. Rev.*, 2015, **115**, 12888–12935.
8 P. V. Kamat, *J. Phys. Chem. C*, 2007, **111**, 2834–2860.
9 M. W. Logan, S. Ayad, J. D. Adamson, T. Dilbeck, K. Hanson and F. J. Uribe-Romo, *J. Mater. Chem. A*, 2017, **5**, 11854–11863.
10 W. Yuan, J. Yuan, J. Xie and C. M. Li, *ACS Appl. Mater. Interfaces*, 2016, **8**, 6082–6092.
11 A. L. Linsebigler, G. Q. Lu and J. T. Yates, *Chem. Rev.*, 1995, **95**, 735–758.
12 Y. J. Wang, Q. S. Wang, X. Y. Zhan, F. M. Wang, M. Safdar and J. He, *Nanoscale*, 2013, **5**, 8326–8339.
13 J.-C. Wang, L. Zhang, W.-X. Fang, J. Ren, Y.-Y. Li, H.-C. Yao, J.-S. Wang and Z.-J. Li, *ACS Appl. Mater. Interfaces*, 2015, **7**, 8631–8639.
14 M. Li, L. Zhang, X. Fan, Y. Zhou, M. Wu and J. Shi, *J. Mater. Chem. A*, 2015, **3**, 5189–5196.
15 W.-N. Wang, F. Wu, Y. Myung, D. M. Niedzwiedzki, H. S. Im, J. Park, P. Banerjee and P. Biswas, *ACS Appl. Mater. Interfaces*, 2015, **7**, 5685–5692.
16 F. Caballero-Briones, J. M. Artes, I. Diez-Perez, P. Gorostiza and F. Sanz, *J. Phys. Chem. C*, 2009, **113**, 1028–1036.
17 L. Yang, S. Luo, Y. Li, Y. Xiao, Q. Kang and Q. Cai, *Environ. Sci. Technol.*, 2010, **44**, 7641–7646.
18 Y. Y. Liu, Y. M. Yang, Q. L. Sun, Z. Y. Wang, B. B. Huang, Y. Dai, X. Y. Qin and X. Y. Zhang, *ACS Appl. Mater. Interfaces*, 2013, **5**, 7654–7658.
19 R. Li, J. Hu, M. Deng, H. Wang, X. Wang, Y. Hu, H.-L. Jiang, J. Jiang, Q. Zhang, Y. Xie and Y. Xiong, *Adv. Mater.*, 2014, **26**, 4783–4788.
20 J. W. Maina, C. Pozo-Gonzalo, L. Kong, J. Schutz, M. Hill and L. F. Dumee, *Mater. Horiz.*, 2017, **4**, 345–361.

21 X. He, Z. Gan, S. Fisenko, D. Wang, H. M. El-Kaderi and W.-N. Wang, *ACS Appl. Mater. Interfaces*, 2017, **9**, 9688–9698.
22 S. Yan, S. Ouyang, H. Xu, M. Zhao, X. Zhang and J. Ye, *J. Mater. Chem. A*, 2016, **4**, 15126–15133.
23 D. Chen, H. Xing, C. Wang and Z. Su, *J. Mater. Chem. A*, 2016, **4**, 2657–2662.
24 S. Liu, F. Chen, S. Li, X. Peng and Y. Xiong, *Appl. Catal., B*, 2017, **211**, 1–10.
25 Q. Liu, Z.-X. Low, L. Li, A. Razmjou, K. Wang, J. Yao and H. Wang, *J. Mater. Chem. A*, 2013, **1**, 11563–11569.
26 A. Crake, K. C. Christoforidis, A. Kafizas, S. Zafeiratos and C. Petit, *Appl. Catal., B*, 2017, **210**, 131–140.
27 L. I. Bendavid and E. A. Carter, *J. Phys. Chem. C*, 2013, **117**, 26048–26059.
28 W. N. Wang, J. Park and P. Biswas, *Catal. Sci. Technol.*, 2011, **1**, 593–600.
29 S. S. Dunkle, R. J. Helmich and K. S. Suslick, *J. Phys. Chem. C*, 2009, **113**, 11980–11983.
30 N. Al-Janabi, P. Hill, L. Torrente-Murciano, A. Garforth, P. Gorgojo, F. Siperstein and X. Fan, *Chem. Eng. J.*, 2015, **281**, 669–677.
31 S. Loera-Serna, M. A. Oliver-Tolentino, M. de Lourdes López-Núñez, A. Santana-Cruz, A. Guzmán-Vargas, R. Cabrera-Sierra, H. I. Beltrán and J. Flores, *J. Alloys Compd.*, 2012, **540**, 113–120.
32 S. Maiti, A. Pramanik, U. Manju and S. Mahanty, *Microporous Mesoporous Mater.*, 2016, **226**, 353–359.
33 K. Jayaramulu, T. Toyao, V. Ranc, C. Rosler, M. Petr, R. Zboril, Y. Horiuchi, M. Matsuoka and R. A. Fischer, *J. Mater. Chem. A*, 2016, **4**, 18037–18042.
34 B. Peng, C. Feng, S. Liu and R. Zhang, *Catal. Today*, DOI: 10.1016/j.cattod.2017.10.044.
35 W. N. Wang, W. J. An, B. Ramalingam, S. Mukherjee, D. M. Niedzwiedzki, S. Gangopadhyay and P. Biswas, *J. Am. Chem. Soc.*, 2012, **134**, 11276–11281.
36 K. Ishibashi, A. Fujishima, T. Watanabe and K. Hashimoto, *Electrochem. Commun.*, 2000, **2**, 207–210.
37 J. C. Wang, L. Zhang, W. X. Fang, J. Ren, Y. Y. Li, H. C. Yao, J. S. Wang and Z. J. Li, *ACS Appl. Mater. Interfaces*, 2015, **7**, 8631–8639.
38 H. Czili and A. Horvath, *Appl. Catal., B*, 2008, **81**, 295–302.
39 E. A. Kraut, R. W. Grant, J. R. Waldrop and S. P. Kowalczyk, *Phys. Rev. Lett.*, 1980, **44**, 1620–1623.
40 S.-M. Park, A. Razzaq, Y. H. Park, S. Sorcar, Y. Park, C. A. Grimes and S.-I. In, *ACS Omega*, 2016, **1**, 868–875.
41 J. Ihli, W. C. Wong, E. H. Noel, Y.-Y. Kim, A. N. Kulak, H. K. Christenson, M. J. Duer and F. C. Meldrum, *Nat. Commun.*, 2014, **5**, 3169.
42 L. Liu, H. Zhao, J. M. Andino and Y. Li, *ACS Catal.*, 2012, **2**, 1817–1828.
43 K. Pokrovski, K. T. Jung and A. T. Bell, *Langmuir*, 2001, **17**, 4297–4303.
44 R. A. Khatri, S. S. C. Chuang, Y. Soong and M. Gray, *Energy Fuels*, 2006, **20**, 1514–1520.
45 L. Liu, C. Zhao, D. Pitts, H. Zhao and Y. Li, *Catal. Sci. Technol.*, 2014, **4**, 1539–1546.
46 R. A. Khatri, S. S. C. Chuang, Y. Soong and M. Gray, *Ind. Eng. Chem. Res.*, 2005, **44**, 3702–3708.
47 L. Liu and Y. Li, *Aerosol Air Qual. Res.*, 2014, **14**, 453–469.
48 S. Kouva, K. Honkala, L. Lefferts and J. Kanervo, *Catal. Sci. Technol.*, 2015, **5**, 3473–3490.
49 K. Teramura, K. Hori, Y. Terao, Z. Huang, S. Iguchi, Z. Wang, H. Asakura, S. Hosokawa and T. Tanaka, *J. Phys. Chem. C*, 2017, **121**, 8711–8721.
50 H. Wu, J. M. Simmons, G. Srinivas, W. Zhou and T. Yildirim, *J. Phys. Chem. Lett.*, 2010, **1**, 1946–1951.
51 S. Chen, T. Cao, Y. Gao, D. Li, F. Xiong and W. Huang, *J. Phys. Chem. C*, 2016, **120**, 21472–21485.
52 S. S.-Y. Chui, S. M.-F. Lo, J. P. Charmant, A. G. Orpen and I. D. Williams, *Science*, 1999, **283**, 1148–1150.
53 L. Liu, C. Zhao and Y. Li, *J. Phys. Chem. C*, 2012, **116**, 7904–7912.
54 X. He, C. Yang, D. Wang, S. E. Gilliland Iii, D.-R. Chen and W.-N. Wang, *CrystEngComm*, 2017, **19**, 2445–2450.
55 S. Bordiga, L. Regli, F. Bonino, E. Groppo, C. Lamberti, B. Xiao, P. S. Wheatley, R. E. Morris and A. Zecchina, *Phys. Chem. Chem. Phys.*, 2007, **9**, 2676–2685.
56 P. D. C. Dietzel, R. E. Johnsen, H. Fjellvag, S. Bordiga, E. Groppo, S. Chavan and R. Blom, *Chem. Commun.*, 2008, 5125–5127, DOI: 10.1039/b810574j.
57 B. Aurian-Blajeni, M. Halmann and J. Manassen, *Sol. Energy*, 1980, **25**, 165–170.
58 B. AlOtaibi, S. Fan, D. Wang, J. Ye and Z. Mi, *ACS Catal.*, 2015, **5**, 5342–5348.
59 J. N. Park and E. W. McFarland, *J. Catal.*, 2009, **266**, 92–97.
60 Y. G. Chen, K. Tomishige, K. Yokoyama and K. Fujimoto, *Appl. Catal., A*, 1997, **165**, 335–347.
61 I. C. Chang, P.-C. Chen, M.-C. Tsai, T.-T. Chen, M.-H. Yang, H.-T. Chiu and C.-Y. Lee, *CrystEngComm*, 2013, **15**, 2363–2366.

Electronic Supporting Information (ESI)

MOF-based Ternary Nanocomposites for Better CO_2 Photoreduction: Roles of Heterojunction and Coordinatively Unsaturated Metal Sites

*Xiang He and Wei-Ning Wang**

Department of Mechanical and Nuclear Engineering, Virginia Commonwealth University, Richmond, Virginia 23219, United States

***Corresponding Author**
Wei-Ning Wang: Tel: 1-(804) 827-4306; Fax: 1-(804) 827-7030; Email: wnwang@vcu.edu

CONTENTS

S1. Characterization of TiO_2 and Cu_2O

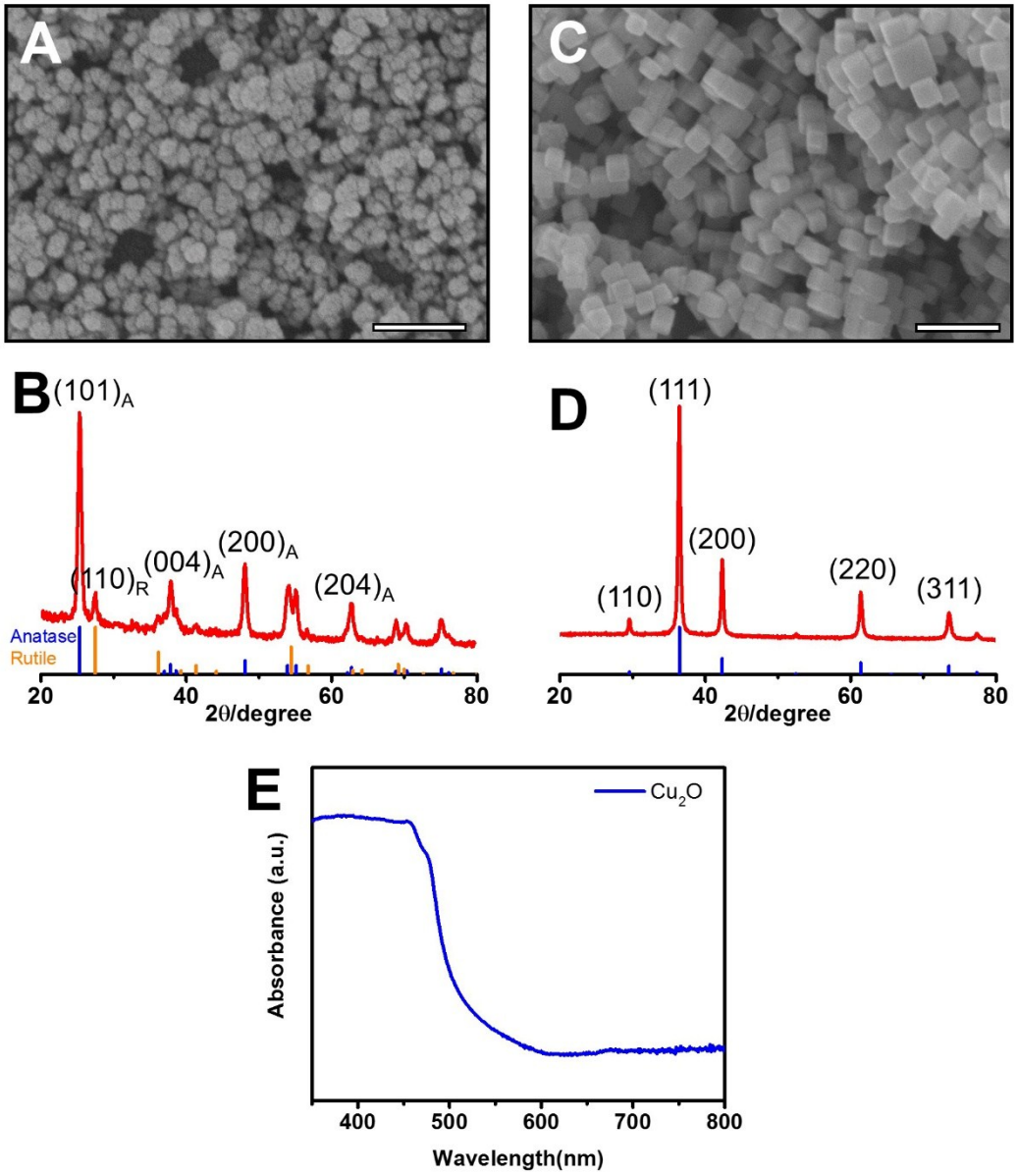

Figure S1. SEM images of (A) P25 and (C) Cu_2O, scale bar: 200 nm; XRD patterns of (B) P25 and (D) Cu_2O; and (E) UV-Visible absorption spectrum of Cu_2O.

The commercial P25 nanoparticles have an irregular shape with an average diameter of 25 nm (**Figure S1A**) and mainly exist as anatase phase with a trace of rutile phase (**Figure S1B**). As shown in **Figure S1C**, the as-synthesized Cu_2O has a cubic shape and has an average diameter of 42 nm. The Cu_2O phase has also been confirmed in **Figure S1D** with the reference (JCPDS 01-071-3645). The Cu_2O nanocubes exhibit broad light absorption from 350 nm to around 500 nm (**Figure S1E**).

S2. Low-magnification SEM Images of As-prepared Samples

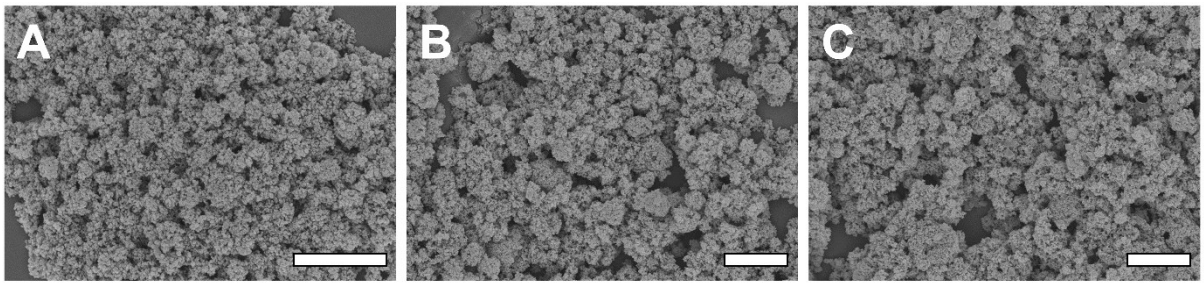

Figure S2. SEM images of (A) sprayed TiO_2, (B) TiO_2/Cu_2O and (C) $TiO_2/Cu_2O/Cu_3(BTC)_2$. Scale bars: 2 μm.

S3. CO_2 Uptake Analysis

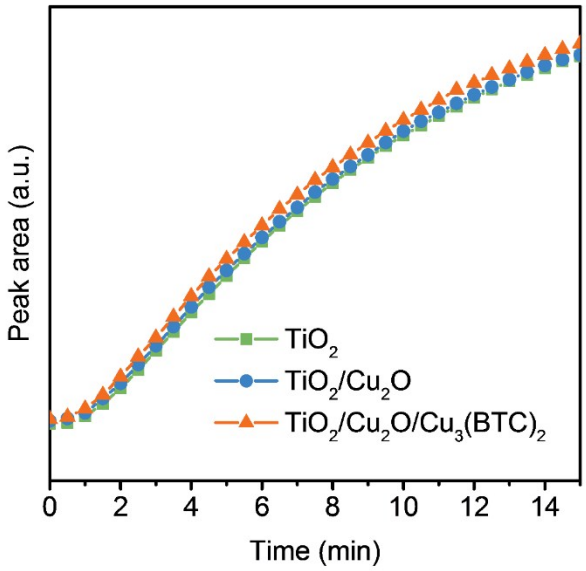

Figure S3. CO_2 uptake analysis by quantifying the area of the characteristic IR peak of adsorbed CO_2 as a function of time during the adsorption process.

The CO_2 adsorption kinetics can be assessed by using DRIFTS, as detailed in our previous studies.[1, 2] In brief, adsorbed CO_2 has characteristic IR peaks in the range of 2280 to 2400 cm^{-1}. The peak areas increase with increased amount of adsorbed CO_2. Thus, CO_2 adsorption kinetics can be obtained by measuring the peak areas from the continuous recorded IR spectra during the CO_2 adsorption process. The CO_2 adsorption results were shown in **Figure S3**, which shows similar CO_2 uptake properties of these three samples, eliminating the effects of CO_2 uptake on the photoreduction efficiency.

S4. Determination of Component Ratios in the Ternary Composite

The component ratios in the ternary composite were determined based on the quantities of the precursors (i.e., TiO_2 and Cu_2O) used for the synthesis and the XPS data of as-prepared ternary composite. To be specific, the molar ratio of TiO_2 to Cu_2O in TiO_2/Cu_2O composite is assumed to be consistent with the precursor TiO_2/Cu_2O molar ratio (i.e., 20:1) used for the synthesis of the binary composite. The binary composite was then used as precursor for the ternary composite after partial conversion of Cu_2O to $Cu_3(BTC)_2$. The percentage of Cu_2O converted to $Cu_3(BTC)_2$ was determined from the XPS analysis of Cu $2p_{3/2}$, where a standard Shirley background and the Gaussian (80%)-Lorentzian (20%) profile were used. As shown in Figure 1N, the Cu $2p_{3/2}$ was further deconvoluted into two peaks centered 932.2 eV and 933.8 eV, originating from Cu^+ in Cu_2O and Cu^{2+} in $Cu_3(BTC)_2$, respectively.[3, 4] From the peak areas, the molar ratio of Cu^+ to Cu^{2+} was determined to be 1.22:1, indicating that $Cu_2O/Cu_3(BTC)_2$ ratio is 1.22:1. Given that the molar ratio of Ti to total Cu is 20:1, the molar ratio of TiO_2, Cu_2O, $Cu_3(BTC)_2$ was determined to be 20: 0.55: 0.45.

S5. CO_2 Photoreduction Analysis

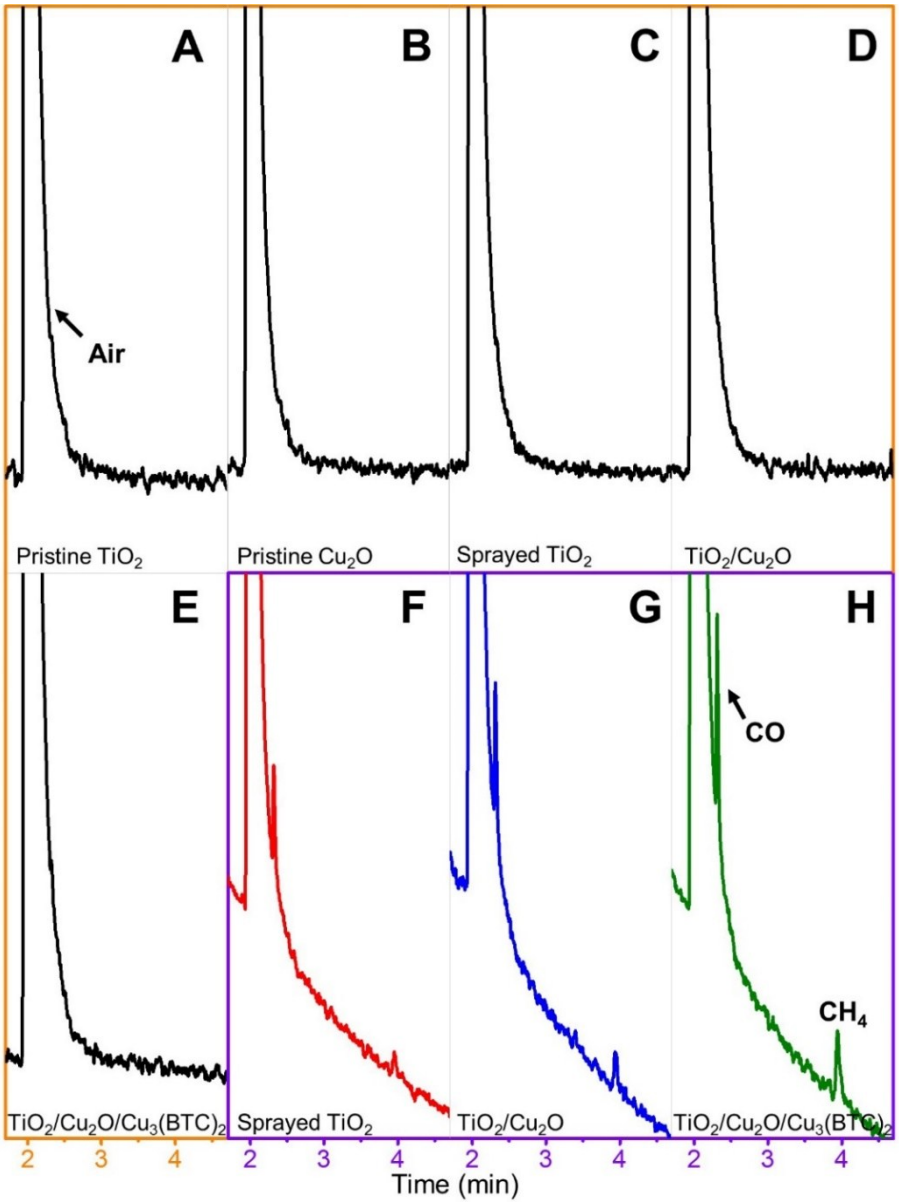

Figure S4. Gas chromatograms attained with samples illuminated at He/water atmosphere (A-E) and CO_2/water atmosphere (F-H). A: Pristine TiO_2; B: Pristine Cu_2O; C and F: Sprayed TiO_2; D and G: TiO_2/Cu_2O; E and H: $TiO_2/Cu_2O/Cu_3(BTC)_2$.

All samples were first subjected to control measurements under helium/water atmosphere to rule out the possibilities of carbon contamination (**Figures S4A-E**), where no CO nor CH_4 peaks are observed for the samples involved, indicating that these samples are carbon contamination-free. Once the CO_2/H_2O mixture was used as the precursor, CO and CH_4 were observed as the major products (**Figures S4F-H**).

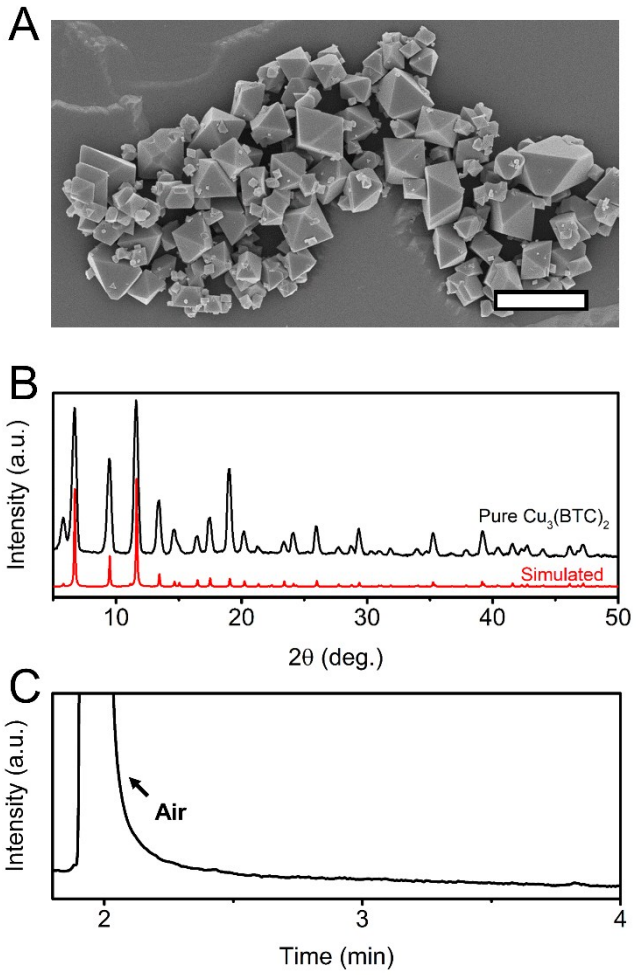

Figure S5. SEM image (A) and XRD pattern (B) of as-prepared pure $Cu_3(BTC)_2$; Gas chromatogram attained with as-prepared pure $Cu_3(BTC)_2$ at CO_2/water atmosphere (C).

In addition, pure $Cu_3(BTC)_2$ was synthesized and subjected to CO_2 photoreduction process in order to determine the role of $Cu_3(BTC)_2$ during the photocatalysis process. The pure $Cu_3(BTC)_2$ was synthesized through the following process. Copper nitrate trihydrate (1.432 g) and trimesic acid (0.842 g) were firstly dissolved in 20 mL dimethylformamide (DMF). The solution was then placed in an oven (80 °C) for 24 hours. After that, the powders were collected by centrifugation, and washed with DMF twice and then methanol twice. Finally, the powder samples were dried overnight in a vacuum oven at 50 °C.

As shown in **Figure S5A**, the as-prepared pure $Cu_3(BTC)_2$ exhibits the characteristic octahedron shape. And the crystal structure of the as-prepared sample was consistent with the simulated pattern of HKUST-1 (**Figure S5B**). Both the SEM and XRD analysis demonstrate that pure $Cu_3(BTC)_2$ crystals have been successfully synthesized. Subsequently, pure $Cu_3(BTC)_2$ was used as the photocatalyst for CO_2 reduction. However, no discernible products were observed (**Figure S5C**) due to the fact that pure $Cu_3(BTC)_2$ is unfavorable for charge separation and can't serve as the photocatalyst for CO_2 reduction. This result is consistent with our previous study[2] and the prior work done by Xiong et al.[5]

S6. Analysis of Cu Valence States after Photocatalysis

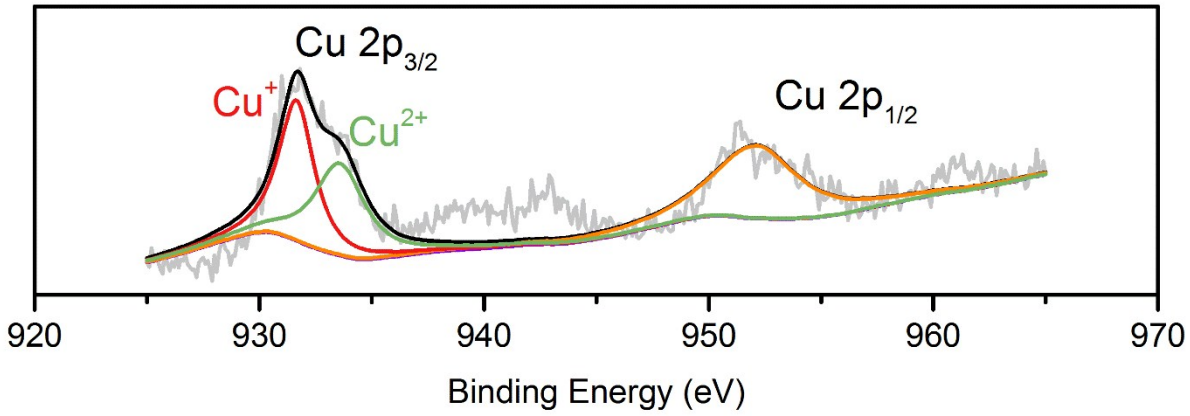

Figure S6. Cu2p XPS spectra of $TiO_2/Cu_2O/Cu_3(BTC)_2$ composite after photocatalysis

S7. Photoluminescence Analysis of·OH Formation

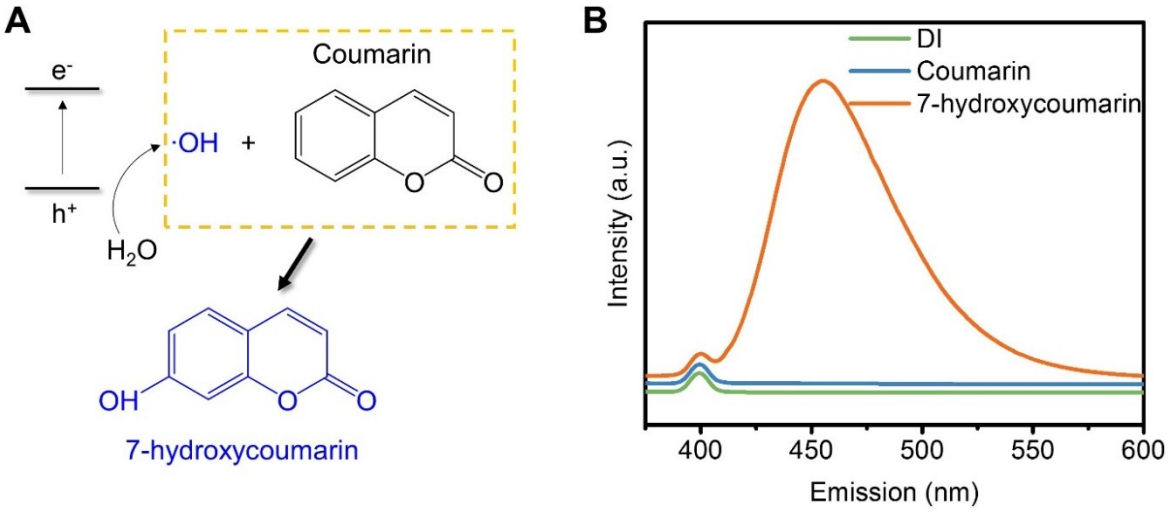

Figure S7. Mechanism of ·OH detection by using coumarin as a probe molecule. (A) Reaction pathway; (B) Emission spectra of various samples. (Concentration of coumarin and 7-hydroxycoumarin: 0.15 μmol/L; Excitation wavelength: 350 nm)

The formation of ·OH, a product from the reaction of holes with water molecules, can be used to monitor the electron/hole pairs generated by the catalysts. The mechanism of ·OH by using coumarin as a probe was illustrated in **Figure S7**. Specifically, coumarin reacts with ·OH to generate 7-hydroxycoumarin (**Figure S7A**),[6] which is highly fluorescent and has a characteristic luminescent emission peak around 455 nm when excited at 350 nm (**Figure S7B**). On the other hand, pure coumarin does not possess any fluorescent properties, as indicated from the identical emission spectra of coumarin and DI water. The emission peak at 397 nm was observed for all the three samples, which is attributed to the Raman scattering of water.[7]

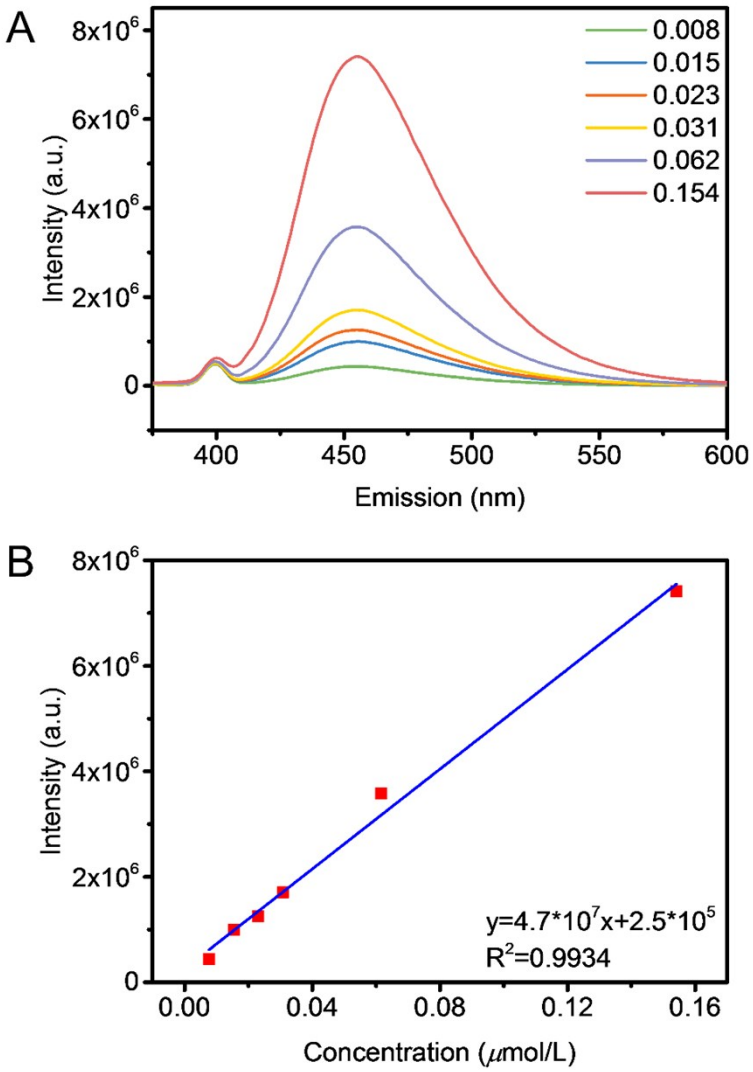

Figure S8. Calibration of PL intensity versus ·OH concentration. (A) Spectra of 7-hydroxycoumarin with various concentrations (μmol/L) (Excitation wavelength: 350 nm); (B) Linear fitting of the experimental data.

Calibration was carried out to quantify the ·OH formation by the photoluminescence peak intensity. In brief, 7-hydroxycoumarin solutions with various concentrations were prepared, and their corresponding emission spectra were obtained at the excitation wavelength of 350 nm (**Figure S8A**). Subsequently, the calibration curve was obtained by correlating the peak intensities with the concentrations (**Figure S8B).** Based on the equation derived from **Figure S8B**, the photogenerated ·OH by TiO_2, TiO_2/Cu_2O and $TiO_2/Cu_2O/Cu_3(BTC)_2$ were quantified to be 0.032, 0.067 and 0.105 μmol/(g·h), respectively. The amount of electron/hole pairs is expected to be the same as that of ·OH because of their stoichiometric relationship. From the information above, the photo-generated electron/hole pairs by TiO_2/Cu_2O and $TiO_2/Cu_2O/Cu_3(BTC)_2$ were calculated to be 2.09 and 3.28 times of those by TiO_2.

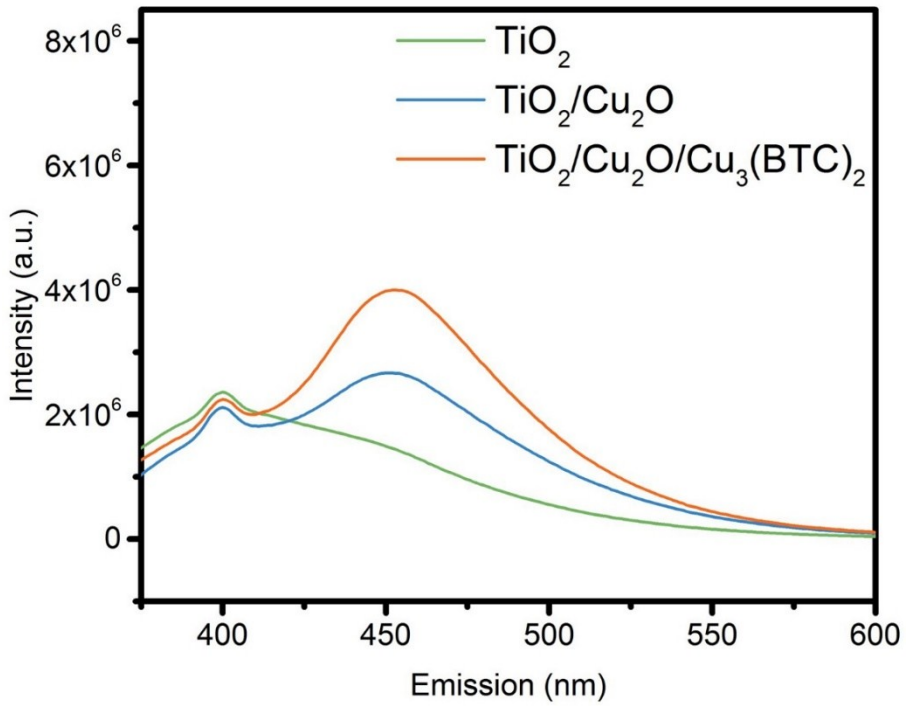

Figure S9. Emission spectra of photo-generated 7-hydroxycoumarin obtained from various samples (Excitation wavelength: 350 nm).

S8. Water Adsorption Analysis

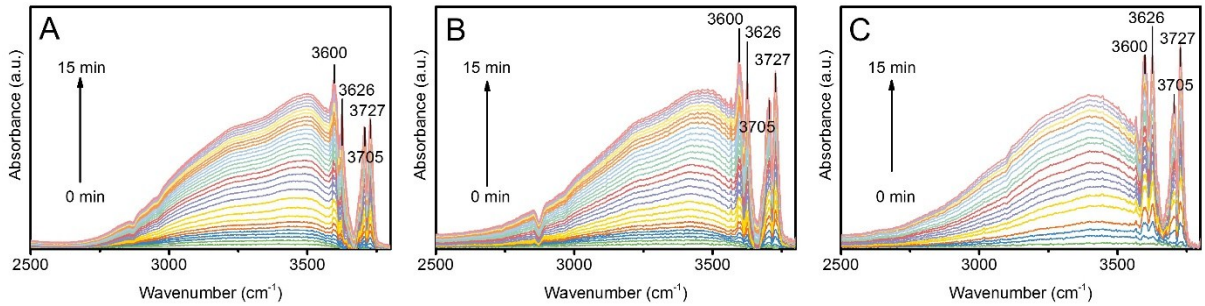

Figure S10. DRIFTS spectra in the range of 2500 to 3800 cm^{-1} obtained during the adsorption of CO_2/water mixture on (A) TiO_2, (B) TiO_2/Cu_2O and (C) $TiO_2/Cu_2O/Cu_3(BTC)_2$.

Figure S10 shows the DRIFTS spectra (2500 to 3800 cm^{-1}) obtained during the adsorption of CO_2/H_2O mixture on the surfaces of the catalysts. In the beginning, no obvious peaks were observed within this range. With prolonged adsorption time, four apparent peaks show up at 3600, 3626, 3705 and 3727 cm^{-1},[8, 9] which can all be assigned to hydroxyl groups, demonstrating the existence of dissociatively chemisorbed water on these three catalysts.[2] Protons, as another product from the dissociation of water, should also exist on the catalyst surface. These protons can react with carbonates to form formate species, which further enhance the photoreduction efficiency.

REFERENCES

1 X. He, C. Yang, D. Wang, S. E. Gilliland Iii, D.-R. Chen and W.-N. Wang, *Crystengcomm*, 2017, **19**, 2445-2450.

2 X. He, Z. Gan, S. Fisenko, D. Wang, H. M. El-Kaderi and W.-N. Wang, *Acs Appl Mater Inter*, 2017, **9**, 9688-9698.

3 K. Jayaramulu, T. Toyao, V. Ranc, C. Rosler, M. Petr, R. Zboril, Y. Horiuchi, M. Matsuoka and R. A. Fischer, *J Mater Chem A*, 2016, **4**, 18037-18042.

4 B. Peng, C. Feng, S. Liu and R. Zhang, *Catal Today*, DOI: https://doi.org/10.1016/j.cattod.2017.10.044.

5 R. Li, J. Hu, M. Deng, H. Wang, X. Wang, Y. Hu, H.-L. Jiang, J. Jiang, Q. Zhang, Y. Xie and Y. Xiong, *Advanced Materials*, 2014, **26**, 4783-4788.

6 K. Ishibashi, A. Fujishima, T. Watanabe and K. Hashimoto, *Electrochem Commun*, 2000, **2**, 207-210.

7 *SN Determination for PTI QuantaMaster™ Fluorometer. Horiba Scientific.*

8 M. I. Zaki and H. Knözinger, *Mater Chem Phys*, 1987, **17**, 201-215.

9 E. J. Heilwell, *Chem Phys Lett*, 1986, **129**, 48-54.